

Score Jacobian Chaining: Lifting Pretrained 2D Diffusion Models for 3D Generation

Haochen Wang^{*1} Xiaodan Du^{*1} Jiahao Li^{*1} Raymond A. Yeh² Greg Shakhnarovich¹

¹TTI-Chicago

²Purdue University

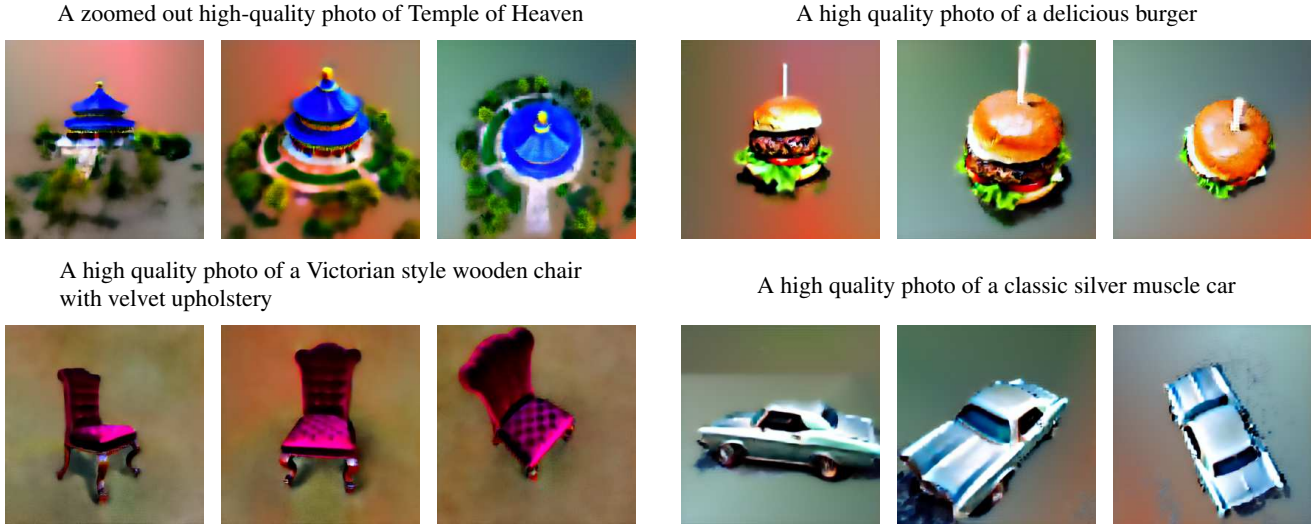


Figure 1. Results for text-driven 3D generation using Score Jacobian Chaining with Stable Diffusion as the pretrained model.

Abstract

A diffusion model learns to predict a vector field of gradients. We propose to apply chain rule on the learned gradients, and back-propagate the score of a diffusion model through the Jacobian of a differentiable renderer, which we instantiate to be a voxel radiance field. This setup aggregates 2D scores at multiple camera viewpoints into a 3D score, and repurposes a pretrained 2D model for 3D data generation. We identify a technical challenge of distribution mismatch that arises in this application, and propose a novel estimation mechanism to resolve it. We run our algorithm on several off-the-shelf diffusion image generative models, including the recently released Stable Diffusion trained on the large-scale LAION 5B dataset.

1. Introduction

We introduce a method that converts a pretrained 2D diffusion generative model on images into a 3D generative model of radiance fields, without requiring access to any 3D data. The key insight is to interpret diffusion models as

learned predictors of a gradient field, often referred to as the *score function* of the data log-likelihood. We apply the chain rule on the estimated score, hence the name Score Jacobian Chaining (SJC).

Following Hyvärinen and Dayan [15], the score is defined as the gradient of the log-density function with respect to the data. Diffusion models of various families [12, 49, 51, 53] can all be interpreted [18, 21, 53] as modeling $\nabla_x \log p_\sigma(x)$ i.e. the denoising score at noise level σ . For readability, we refer to the denoising score as the score. Generating a sample from a diffusion model involves repeated evaluations of the score function from large to small σ level, so that a sample x gradually moves closer to the data manifold. It can be loosely interpreted as gradient descent, with precise control on the step sizes so that data distribution evolves to match the annealed σ level (ancestral sampler [12], SDE and probability-flow ODE [53], etc.). While there are other perspectives to a diffusion model [12, 49], here we are primarily motivated from the viewpoint that diffusion models produce a gradient field.

A natural question to ask is whether the chain rule can be applied to the learned gradients. Consider a diffusion model on images. An image x may be parameterized by some

* Equal contribution.

function f with parameters θ , *i.e.*, $x = f(\theta)$. Applying the chain rule through the Jacobian $\frac{\partial x}{\partial \theta}$ converts a gradient on image x into a gradient on the parameter θ . There are many potential use cases for pairing a pretrained diffusion model with different choices of f . In this work we are interested in exploring the connection between 3D and multiview 2D by choosing f to be a differentiable renderer, thus creating a 3D generative model using only pretrained 2D resources.

Many prior works [2, 58, 60] perform 3D generative modeling by training on 3D datasets [5, 23, 55, 59]. This approach is often as challenging as it is format-ambiguous. In addition to the high data acquisition cost of 3D assets [9], there is no universal data format: point clouds, meshes, volumetric radiance field, etc, all have computational trade-offs. What is common to these 3D assets is that they can be rendered into 2D images. An inverse rendering system, or a differentiable renderer [24, 26, 29, 34, 39], provides access to the Jacobian $J_\pi \triangleq \frac{\partial x_\pi}{\partial \theta}$ of a rendered image x_π at camera viewpoint π with respect to the underlying 3D parameterization θ . Our method uses differentiable rendering to aggregate 2D image gradients over multiple viewpoints into a 3D asset gradient, and lifts a generative model from 2D to 3D. We parameterize a 3D asset θ as a radiance field stored on voxels and choose f to be the volume rendering function.

A key technical challenge is that computing the 2D score by directly evaluating a diffusion model on a rendered image x_π leads to an out-of-distribution (OOD) problem. Generally, diffusion models are trained as denoisers and have only seen noisy inputs during training. On the other hand, our method requires evaluating the denoiser on non-noisy rendered images from a 3D asset during optimization, and it leads to the OOD problem. To address the issue, we propose *Perturb-and-Average Scoring*, an approach to estimate the score for non-noisy images.

Empirically, we first validate the effectiveness of *Perturb-and-Average Scoring* at solving the OOD problem and explore the hyperparameter choices on a simple 2D image canvas. Here we identify open problems on using unconditioned diffusion models trained on FFHQ and LSUN Bedroom. Next, we use Stable Diffusion, a model pretrained on the web-scale LAION dataset to perform SJC for 3D generation, as shown in Fig. 1. **Our contributions are as follows:**

- We propose a method for lifting a 2D diffusion model to 3D via an application of the chain rule.
- We illustrate the challenge of OOD when using a pretrained denoiser and propose *Perturb-and-Average Scoring* to resolve it.
- We point out the subtleties and open problems on applying *Perturb-and-Average Scoring* as gradient for optimization.
- We demonstrate the effectiveness of SJC for the task of 3D text-driven generation.

2. Related Works

Diffusion models have recently advanced to image generation on Internet-scale datasets [10, 36, 42, 44–47]. A diffusion model could be interpreted as either a VAE [12, 49] or a denoising score-matcher [51, 53, 56]. Notably, models trained under one regime can be directly used for inference and sampling by the other [18, 53]; they are in practice largely equivalent.

Neural radiance fields (NeRF) is a family of inverse rendering algorithms that have excelled at multiview 3D reconstruction tasks including view synthesis and surface geometry estimation [31, 34, 40, 57, 61]. Conceptually, a 3D asset is represented as a dense grid of RGB colors and spatial density τ , and rendered into images in a way analogous to alpha compositing [32]. NeRF parameterizes the (RGB, τ) volume with a neural network, but querying the network densely in 3D incurs significant compute costs. Alternatively, Voxel NeRFs [6, 27, 54, 62] store the volume on voxels and observe no loss in end task performance [54, 62]. Querying voxels is a simple memory operation that is much faster than a feedforward pass of a neural network. Here we use a customized voxel radiance field with hyperparameters based on DvGO [54] and TensoRF [6].

2D-supervised 3D GANs pioneered [35, 43, 64] the approach of training 3D generative models using only unstructured 2D images, and promise greater scalability in terms of data. Rather than supervising directly on the 3D asset a model generates, these methods supervise the 2D renderings of the generated 3D asset, often using an adversarial loss [3, 4, 38, 48, 65]. In other words, only images are needed as training data. However, training such a 3D generative model from scratch is still challenging [37]. Recent empirical evaluation remains mostly on human and animal faces [3]. Our method does the opposite: we take an image generative model that is *already pretrained* on large amounts of 2D data and use it to guide the iterative optimization of a 3D asset. Optimization-based generation makes it much slower compared to 3D GANs, but it becomes possible to harness powerful off-the-shelf 2D generative models such as Stable Diffusion [45] for greater content diversity.

CLIP-guided, optimization-based 3D generative models share a similar philosophy of optimizing 3D assets by guiding on 2D renderings [14, 16, 17, 20, 25, 33]. Among them, DreamFields [16] and PureClipNeRF [25] also use NeRF as their differentiable renderers. In this case, the 2D guidance comes from CLIP [42], a pretrained image-text matching model. These works optimize the 3D assets so that the image renderings match a user-provided text prompt. Since CLIP is not a 2D generative model per se, such a pipeline usually creates some abstract distilled content [28] that looks very different from real images. In contrast, we use diffusion models, which are proper 2D generative models, to create

realistic looking 3D content.

DreamFusion. The recently arXived work by Poole et al. [41], *independent and concurrent to our work*, proposes an algorithm that is similar to our approach at the pseudo-code level. Differently, their procedure uses the mathematical setup by Graikos et al. [11] to search for image parametrization that minimizes the training loss of a diffusion model. In contrast, our work is motivated by applying the chain rule to the 2D score. The key differences have been summarized in Sec. 4.3. In terms of implementation, we do not have access to the close-sourced Imagen [46] diffusion model. Instead, we use the pretrained Stable Diffusion model released by Rombach et al. [45]. For a comparison with DreamFusion, we use with a third-party implementation based on the same diffusion model, namely Stable-DreamFusion.

3. Preliminaries

To establish a common notation, we briefly review the score-based perspective of diffusion models. For readers familiar with VAE literature on diffusion models, we provide a concise score-based formula card and more details in Appendix Sec. A1 to connect these ideas.

Denoising score matching. Given a dataset of samples $\mathcal{Y} = \{\mathbf{y}_i\}$ drawn from p_{data} , a diffusion model revolves primarily around learning a denoiser D by minimizing the difference between a noised sample $\mathbf{y} + \sigma \mathbf{n}$ and \mathbf{y} ,

$$\mathbb{E}_{\mathbf{y} \sim p_{\text{data}}} \mathbb{E}_{\mathbf{n} \sim \mathcal{N}(0, \mathbf{I})} \|D(\mathbf{y} + \sigma \mathbf{n}; \sigma) - \mathbf{y}\|_2^2, \quad (1)$$

i.e. D is denoising the input $\mathbf{y} + \sigma \mathbf{n}$, for a range of σ values. For 2D images, D is commonly chosen to be a ConvNet. Variants such as DDPM [12] parameterized the ConvNet to instead predict a noise residual $\hat{\epsilon}$, and these models can be converted back to the form of a denoiser by [53]

$$D(\mathbf{x}; \sigma) = \mathbf{x} - \sigma \hat{\epsilon}(\mathbf{x}). \quad (2)$$

In this paper, we treat all pretrained diffusion models as denoisers, and perform the interface conversion in our implementation when needed.

Score from denoiser. Let $p_\sigma(\mathbf{x})$ denote the data distribution perturbed by Gaussian noise of standard deviation σ . It is shown in prior works [15, 51] that the denoiser D trained according to Eq. (1) provides a good approximation to the denoising score:

$$\nabla_{\mathbf{x}} \log p_\sigma(\mathbf{x}) \approx \frac{D(\mathbf{x}; \sigma) - \mathbf{x}}{\sigma^2}. \quad (3)$$

A denoising diffusion model estimates the *score function* of the noised distribution $p_\sigma(\mathbf{x})$ at various $\sigma \in \{\sigma_i\}_{i=1}^T$. To perform sampling, the diffusion model gradually updates a

sample through a sequence of noise levels of $\sigma_T > \dots > \sigma_0 = 0$. $\{\sigma_i\}$ are chosen empirically, with a typical range being [0.01, 157] [12] in the case of DDPM.

Score as mean-shift. A helpful intuition is that the score behaves like *mean-shift* [7, 8]. If we simplify p_{data} to be an empirical data distribution over the i.i.d. samples $\{\mathbf{y}_i\}$, then at noise level σ , $p_\sigma(\mathbf{x})$ takes the form of a mixture of Gaussians [52]

$$p_\sigma(\mathbf{x}) = \mathbb{E}_{\mathbf{y} \sim p_{\text{data}}} \mathcal{N}(\mathbf{x}; \mathbf{y}, \sigma^2 \mathbf{I}). \quad (4)$$

In this case there exists a closed-form expression [18, 52] to the optimal denoiser

$$D(\mathbf{x}; \sigma) = \frac{\sum_i \mathcal{N}(\mathbf{x}; \mathbf{y}_i, \sigma^2 \mathbf{I}) \mathbf{y}_i}{\sum_i \mathcal{N}(\mathbf{x}; \mathbf{y}_i, \sigma^2 \mathbf{I})}. \quad (5)$$

In other words, $D(\mathbf{x}; \sigma)$ is a locally weighted mean of data samples $\{\mathbf{y}_i\}$ around \mathbf{x} under a Gaussian kernel with bandwidth σ . The denoising score function can be thought of as a non-parametric guide on how to update \mathbf{x} in order to move it towards its *weighted nearest neighbors*.

4. Score Jacobian Chaining for 3D Generation

Let $\boldsymbol{\theta}$ denotes the parameters of a 3D asset, e.g., voxel grid of (RGB, τ) as in Sec. 4.2. Our goal is to model and sample from the distribution $p(\boldsymbol{\theta})$ to generate a 3D scene. In our setting, only a pretrained 2D diffusion model on images $p(\mathbf{x})$ is given and we do not have access to 3D data. To relate the 2D and 3D distributions $p(\mathbf{x})$ and $p(\boldsymbol{\theta})$, we assume that the probability density of 3D asset $\boldsymbol{\theta}$ is proportional to the expected probability densities of its multiview 2D image renderings \mathbf{x}_π over camera poses π , i.e.,

$$p_\sigma(\boldsymbol{\theta}) \propto \mathbb{E}_\pi [p_\sigma(\mathbf{x}_\pi(\boldsymbol{\theta}))], \quad (6)$$

up to a normalization constant $Z = \int \mathbb{E}_\pi [p_\sigma(\mathbf{x}_\pi(\boldsymbol{\theta}))] d\boldsymbol{\theta}$. That is, a 3D asset $\boldsymbol{\theta}$ is as likely as its 2D renderings \mathbf{x}_π .

Next, we establish a lower bound, $\log \tilde{p}_\sigma(\boldsymbol{\theta})$, on the distribution in Eq. (6) using Jensen's inequality:

$$\log p_\sigma(\boldsymbol{\theta}) = \log [\mathbb{E}_\pi (p_\sigma(\mathbf{x}_\pi))] - \log Z \quad (7)$$

$$\geq \mathbb{E}_\pi [\log p_\sigma(\mathbf{x}_\pi)] - \log Z \triangleq \log \tilde{p}_\sigma(\boldsymbol{\theta}). \quad (8)$$

Recall that the score is the *gradient* of log probability density of data. By chain rule

$$\nabla_{\boldsymbol{\theta}} \log \tilde{p}_\sigma(\boldsymbol{\theta}) = \mathbb{E}_\pi [\nabla_{\boldsymbol{\theta}} \log p_\sigma(\mathbf{x}_\pi)] \quad (9)$$

$$\frac{\partial \log \tilde{p}_\sigma(\boldsymbol{\theta})}{\partial \boldsymbol{\theta}} = \mathbb{E}_\pi \left[\frac{\partial \log p_\sigma(\mathbf{x}_\pi)}{\partial \mathbf{x}_\pi} \cdot \frac{\partial \mathbf{x}_\pi}{\partial \boldsymbol{\theta}} \right] \quad (10)$$

$$\underbrace{\nabla_{\boldsymbol{\theta}} \log \tilde{p}_\sigma(\boldsymbol{\theta})}_{\text{3D score}} = \mathbb{E}_\pi \left[\underbrace{\nabla_{\mathbf{x}_\pi} \log p_\sigma(\mathbf{x}_\pi)}_{\text{2D score; pretrained}} \cdot \underbrace{\mathbf{J}_\pi}_{\text{renderer Jacobian}} \right]. \quad (11)$$

We will next discuss how to compute the 2D score in practice using a pretrained diffusion model.

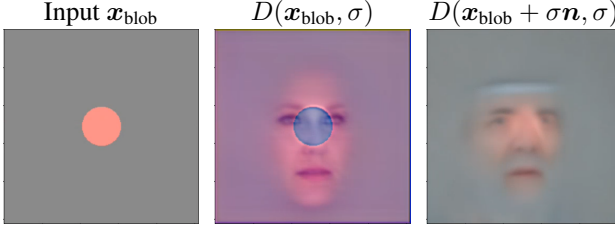


Figure 2. Illustration of denoiser’s OOD issue using a denoiser pre-trained on FFHQ. When directly evaluating $D(\mathbf{x}_{\text{blob}}, \sigma)$ the model did not correct for the orange blob into a face image. Contrarily, evaluating the denoiser on noised input $D(\mathbf{x}_{\text{blob}} + \sigma \mathbf{n}, \sigma)$ produces an image that successfully merges the blob with the face manifold.

4.1. Computing 2D Score on Non-Noisy Images

Computing the 3D score in Eq. (11) requires the 2D score on \mathbf{x}_π . A first attempt would be to directly apply the score from the denoiser in Eq. (3), i.e.,

$$\text{score}(\mathbf{x}_\pi, \sigma) \triangleq (D(\mathbf{x}_\pi; \sigma) - \mathbf{x}_\pi)/\sigma^2. \quad (12)$$

Unfortunately, evaluating the pretrained denoiser D on \mathbf{x}_π causes an out-of-distribution (OOD) problem. From the training objective in Eq. (1), at each noise level σ , the denoiser D has only seen noisy inputs of the distribution $\mathbf{y} + \sigma \mathbf{n}$ where $\mathbf{y} \sim p_{\text{data}}$ and $\mathbf{n} \sim \mathcal{N}(0, \mathbf{I})$. However, a rendered image \mathbf{x}_π from 3D asset θ is generally not consistent with such distribution.

We illustrate this OOD situation in Fig. 2. Given a denoiser pretrained on FFHQ [19] by Baranckuk et al. [1], we visualize the output $D(\mathbf{x}_{\text{blob}}; \sigma = 6.5)$ where the input \mathbf{x}_{blob} is a non-noisy image showing an orange blob centered on a grey canvas. Under the intuition that D predicts a *weighted nearest neighbor* as reviewed in (5), we expect the denoiser to blend the orange blob with the manifold of faces. However in reality we observe sharp artifacts when updating with this score $(D(\mathbf{x}_{\text{blob}}; \sigma) - \mathbf{x}_{\text{blob}})/\sigma^2$ and the image becomes further away from the face manifold.

Perturb-and-Average Scoring. To address the OOD problem, we propose *Perturb-and-Average Scoring* (PAAS). It computes the score on non-noisy images \mathbf{x}_π with a denoiser D by adding noise to the input, and then considering the expectation of the predicted scores w.r.t. the random noise,

$$\text{PAAS}(\mathbf{x}_\pi, \sqrt{2}\sigma) \quad (13)$$

$$\triangleq \mathbb{E}_{\mathbf{n} \sim \mathcal{N}(0, \mathbf{I})} [\text{score}(\mathbf{x}_\pi + \sigma \mathbf{n}, \sigma)] \quad (14)$$

$$= \mathbb{E}_{\mathbf{n}} \left[\frac{D(\mathbf{x}_\pi + \sigma \mathbf{n}, \sigma) - (\mathbf{x}_\pi + \sigma \mathbf{n})}{\sigma^2} \right] \quad (15)$$

$$= \mathbb{E}_{\mathbf{n}} \left[\frac{D(\mathbf{x}_\pi + \sigma \mathbf{n}, \sigma) - \mathbf{x}_\pi}{\sigma^2} \right] \underbrace{- \mathbb{E}_{\mathbf{n}} \left[\frac{\mathbf{n}}{\sigma} \right]}_{=0}. \quad (16)$$

In practice, we use the Monte Carlo estimate of the expectation in Eq. (16). The algorithm is illustrated in Fig. 3. Given

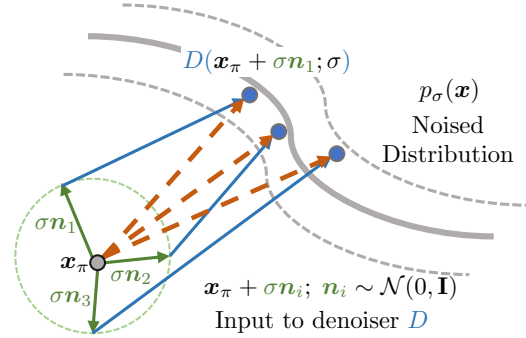


Figure 3. Computing PAAS on 2D renderings \mathbf{x}_π . Directly evaluating $D(\mathbf{x}_\pi; \sigma)$ leads to an OOD problem. Instead, we add noise to \mathbf{x}_π , and evaluate $D(\mathbf{x}_\pi + \sigma \mathbf{n}; \sigma)$ (blue dots). The PAAS is then computed by averaging over the brown dashed arrows, corresponding to multiple samples of \mathbf{n} . See Sec. 4.1 for details.

a set of sampled noises $\{\mathbf{n}_i\}$, each $D(\mathbf{x}_\pi + \sigma \mathbf{n}_i)$ provides an update direction on the perturbed input $\mathbf{x}_\pi + \sigma \mathbf{n}_i$. By averaging over the noise perturbations $\{\mathbf{n}_i\}$, we obtain an update direction on \mathbf{x}_π itself.

Justifying PAAS in Eq. (13). We show that Perturb-and-Average Scoring provides an approximation to the score on \mathbf{x}_π at an inflated noise level of $\sqrt{2}\sigma$

$$\text{PAAS}(\mathbf{x}_\pi, \sqrt{2}\sigma) \approx \nabla_{\mathbf{x}_\pi} \log p_{\sqrt{2}\sigma}(\mathbf{x}_\pi). \quad (17)$$

Lemma 1 Assuming an empirical data distribution $p_\sigma(\mathbf{x})$ in Eq. (4), for any $\mathbf{x} \in \mathbb{R}^d$

$$\log p_{\sqrt{2}\sigma}(\mathbf{x}) \geq \mathbb{E}_{\mathbf{n} \sim \mathcal{N}(0, \mathbf{I})} \log p_\sigma(\mathbf{x} + \sigma \mathbf{n}). \quad (18)$$

Proof. Observe that the LHS of Eq. (19) is a convolution of two Gaussians, therefore

$$\mathbb{E}_{\mathbf{n} \sim \mathcal{N}(0, \mathbf{I})} [\mathcal{N}(\mathbf{x} + \sigma \mathbf{n}; \boldsymbol{\mu}, \sigma^2 \mathbf{I})] = \mathcal{N}(\mathbf{x}; \boldsymbol{\mu}, 2\sigma^2 \mathbf{I}) \quad (19)$$

Recall that $p_\sigma(\mathbf{x})$ is a mixture of Gaussians per Eq. (4);

$$p_{\sqrt{2}\sigma}(\mathbf{x}) = \mathbb{E}_{\mathbf{y} \sim p_{\text{data}}} \mathcal{N}(\mathbf{x}; \mathbf{y}, 2\sigma^2 \mathbf{I}) \quad (20)$$

$$= \mathbb{E}_{\mathbf{y} \sim p_{\text{data}}} \mathbb{E}_{\mathbf{n} \sim \mathcal{N}(0, \mathbf{I})} \mathcal{N}(\mathbf{x} + \sigma \mathbf{n}; \mathbf{y}, \sigma^2 \mathbf{I}) \quad (21)$$

$$= \mathbb{E}_{\mathbf{n} \sim \mathcal{N}(0, \mathbf{I})} \mathbb{E}_{\mathbf{y} \sim p_{\text{data}}} \mathcal{N}(\mathbf{x} + \sigma \mathbf{n}; \mathbf{y}, \sigma^2 \mathbf{I}) \quad (22)$$

$$= \mathbb{E}_{\mathbf{n} \sim \mathcal{N}(0, \mathbf{I})} p_\sigma(\mathbf{x} + \sigma \mathbf{n}). \quad (23)$$

Taking the log on both sides of Eq. (23) and by Jensen’s inequality, we arrive at Eq. (18). \square

Claim 1 Assuming a trained denoiser D as in Eq. (3), our $\text{PAAS}(\mathbf{x}_\pi, \sqrt{2}\sigma)$ in Eq. (13) computes the gradient w.r.t. a lower bound of $\log p_{\sqrt{2}\sigma}(\mathbf{x})$.

Proof. By taking the gradient of the RHS of Lemma 1,

$$\begin{aligned} \nabla_{\mathbf{x}} \mathbb{E}_{\mathbf{n}} \log p(\mathbf{x} + \sigma \mathbf{n}, \sigma) &= \mathbb{E}_{\mathbf{n}} \nabla_{\mathbf{x} + \sigma \mathbf{n}} \log p_\sigma(\mathbf{x} + \sigma \mathbf{n}) \\ &= \mathbb{E}_{\mathbf{n}} [\text{score}(\mathbf{x}_\pi + \sigma \mathbf{n}, \sigma)]. \end{aligned} \quad (24)$$

which is the proposed PAAS algorithm in Eq. (13). \square

4.2. Inverse Rendering on Voxel Radiance Field

With the computation of the 2D score resolved, the other half of our setup in Eq. (11) requires access to the Jacobian of a differentiable renderer.

3D Representation. We represent a 3D asset θ as a voxel radiance field [6, 54, 62], which is much faster to access and update compared to a vanilla NeRF parameterized by a neural network [34]. The parameters θ consist of a density voxel grid $\mathbf{V}^{(\text{density})} \in \mathbb{R}^{1 \times N_x \times N_y \times N_z}$ and a voxel grid of appearance features $\mathbf{V}^{(\text{app})} \in \mathbb{R}^{c \times N_x \times N_y \times N_z}$. Conventionally the appearance features are simply the RGB colors and $c = 3$. For simplicity, we do not model view dependencies in this work.

Inverse Volumetric Rendering. Image rendering is performed independently along a camera ray through each pixel. We cut a camera light ray into equally distanced segments of length d , and at the spatial location corresponding to the beginning of the i -th segment we sample a (RGB_i, τ_i) tuple from the color and density grids using trilinear interpolation. These values are alpha-composited using volume rendering quadrature [32] into the pixel color $C = \sum_i w_i \cdot \text{RGB}_i$, where

$$w_i = \alpha_i \cdot \prod_{j=0}^{i-1} (1 - \alpha_j); \quad \alpha_i = 1 - \exp(-\tau_i d). \quad (25)$$

Volume rendering of θ is directly differentiable. At a rendered image \mathbf{x}_π , the Vector-Jacobian product in Eq. (11) between $\text{PAAS}(\mathbf{x}_\pi)$ and the Jacobian $J_\pi = \frac{\partial \mathbf{x}_\pi}{\partial \theta}$ is computed by back-propagating the score through Eq. (25). This Vector-Jacobian product provides us with the 3D gradient needed for generative modeling on the voxel radiance field.

Regularization Strategies. The voxel grid is a very powerful 3D representation for volumetric rendering. Given noisy 2D guidance, the model may cheat by populating the entire grid with small densities such that the combined effect from one view hallucinates a plausible image. We propose several techniques to encourage the formation of a coherent 3D structure.

Emptiness Loss: Ideally, the space should be sparse with near zero densities except at the object. We propose an emptiness loss to encourage sparsity on a ray \mathbf{r} :

$$\mathcal{L}_{\text{emptiness}}(\mathbf{r}) = \frac{1}{N} \sum_{i=1}^N \log(1 + \beta \cdot w_i), \quad (26)$$

where w_i are the alpha-composited weights shown in (25). The shape of the log function imposes severe penalties at the onset of small weights, but does not grow aggressively if the weights are large. It is consistent with our aim to eliminate small densities. The hyperparameter β controls the steepness of the loss function near 0. A larger β will put more emphasis on eliminating low-density noise. We set $\beta = 10$.

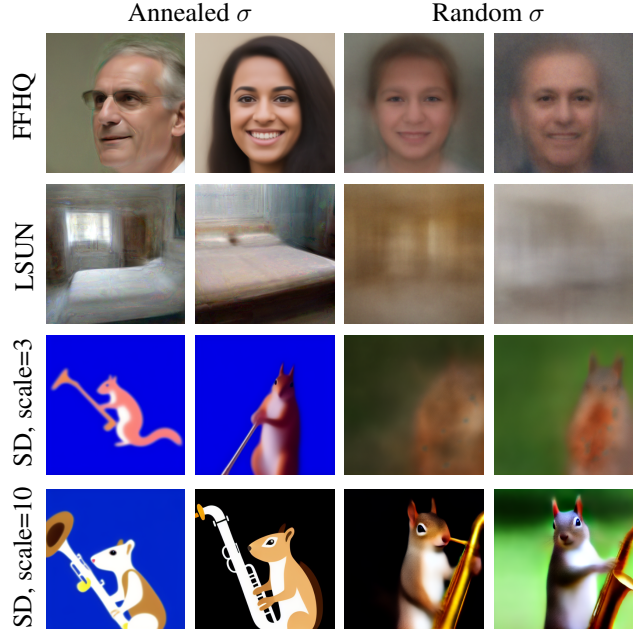


Figure 4. Sampling 2D images with Perturb-and-Average Scoring. We compare Annealed vs Random σ schedule against several diffusion models. Row 1 & 2: the random σ schedule exhibits strong mode-seeking behavior, and it results in low-quality “mean” images on unconditioned diffusion models trained on FFHQ and LSUN Bedroom. In this case, we need a carefully designed annealed σ schedule to produce better, more diverse samples. Row 3 & 4: Stable Diffusion (SD) is conditioned on the prompt “a squirrel holding a saxophone”. The use of natural language makes the conditioned distribution much easier to sample from. When the guidance scale is elevated to 10, Random σ schedule that fails on FFHQ and LSUN starts to produce crisp, clean images.

Emptiness Loss Schedule: We use a hyperparameter λ to control the contribution of the emptiness loss. If we apply a large emptiness loss, it will hinder the learning of geometry in the early stage of training. But if the emptiness is too small, there will be floating density artifacts. We adopt a two-stage noise elimination schedule to deal with this problem. In the first K iterations, we use a relatively small weighting factor λ_1 . After the K^{th} iteration, it is increased to a larger λ_2 . In our experiments $\lambda_1 = 1 \times 10^4$ and $\lambda_2 = 2 \times 10^5$. We provide an ablation study of this technique in Fig. 7 to show its effectiveness.

Center Depth Loss: Sometimes the optimization places the object away from the scene center. The object either becomes small or wander around the image boundary. For the few cases when this happens we apply a center depth loss

$$\mathcal{L}_{\text{center}}(\mathbf{D}) = -\log \left(\frac{1}{|\mathcal{B}|} \sum_{\mathbf{p} \in \mathcal{B}} \mathbf{D}(\mathbf{p}) - \frac{1}{|\mathcal{B}^C|} \sum_{\mathbf{q} \notin \mathcal{B}} \mathbf{D}(\mathbf{q}) \right) \quad (27)$$

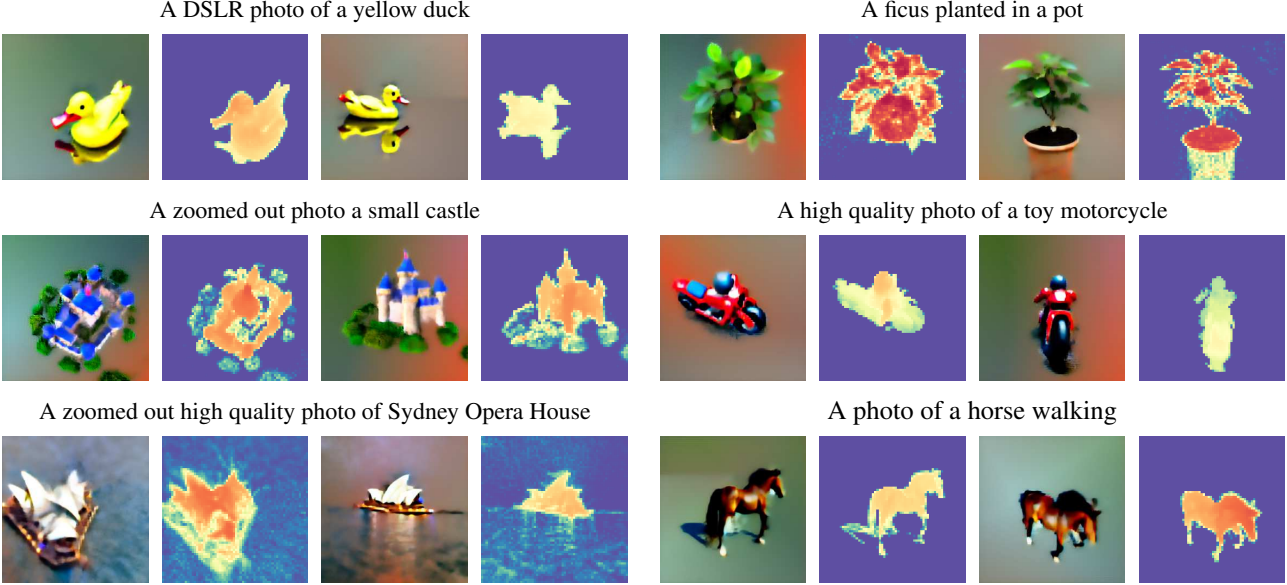


Figure 5. Qualitative results of text-prompted generation of 3D models with SJC, purely from the pretrained Stable Diffusion (2D) image model. Each row shows two views, with associated depth maps (blue is far, red is near), for a single 3D model generated for a given prompt. Note the detailed appearance as well as a sharp, well-defined depth structure.

where D is the depth image, \mathcal{B} is a box (set of pixel locations) at the center of the image, and \mathcal{B}^C is its complement.

4.3. SJC vs. DreamFusion

In this section, we describe the differences and the connections between our SJC and DreamFusion.

Differences from DreamFusion. In terms of formulation, DreamFusion’s computation of the gradient w.r.t. θ involves a U-Net Jacobian term (see Eq. 2 in their paper [41]). In practice, they “found that omitting the U-Net Jacobian term” to be more effective. On the other hand, this U-Net Jacobian term *does not appear* in our formulation. Their additional justification in the appendix actually leans more towards our viewpoint. An additional contribution of ours beyond DreamFusion [41] is our analysis of the effect that the OOD problem has when using a denoiser on rendered images (Claim 1), and the PAAS method to address it. For the variance reduction technique, namely the use of the Monte-Carlo estimate on Eq. (16), or $\hat{\epsilon} - \epsilon$ (in DreamFusion), vs. on Eq. (15), we observe comparable performance between the two methods empirically for 3D generation.

Influences by DreamFusion. At the time of this submission, DreamFusion is a concurrent arXiv paper. However, as we have read the paper, our research was influenced by their reported observations. In particular, we adopted the idea of randomized scheduling of σ during 3D optimization for easier hyperparameter tuning, and used view-augmented language prompting that improves the overall 3D quality. For future work we do hope to explore a more general solution than view-dependent prompts.

5. Experiments

We conduct experiments on both unconditioned and conditioned diffusion models to have a more comprehensive understanding of the properties of SJC.

DDPMs trained on FFHQ and LSUN Bedroom are unconditioned diffusion models with an architecture based on the implementation by Dhariwal and Nichol [10]. They are trained on an image resolution of 256×256 . FFHQ [19] is a dataset of aligned faces with diverse coverage of gender, age, race, facial appearance as well as head poses. LSUN Bedroom [63] includes bedroom images with varied furniture layout plans and rich interior design styles.

Stable Diffusion is an expanded work based on Latent Diffusion Model (LDM) developed by Rombach et al. [45]. It is trained on the LAION5B dataset [47]. We use the release version v1.5. Diffusion is performed on a latent space of $4 \times 64 \times 64$, then upsampled to $3 \times 256 \times 256$ by a decoder. The model is natively trained for text-conditioned image generations, and exposes a guidance scale parameter that controls the strength of language conditioning [13]. Intuitively a larger guidance scale makes the conditioned image distribution more faithful to the text prompt by trading off sample diversity.

5.1. Validating PAAS on 2D images.

Before directly jumping to 3D generation, we first verify that PAAS provides effective guidance on a simple 2D image canvas. In other words, here θ is a grid of RGB values and f is an identity function. The hope is that gradient descent

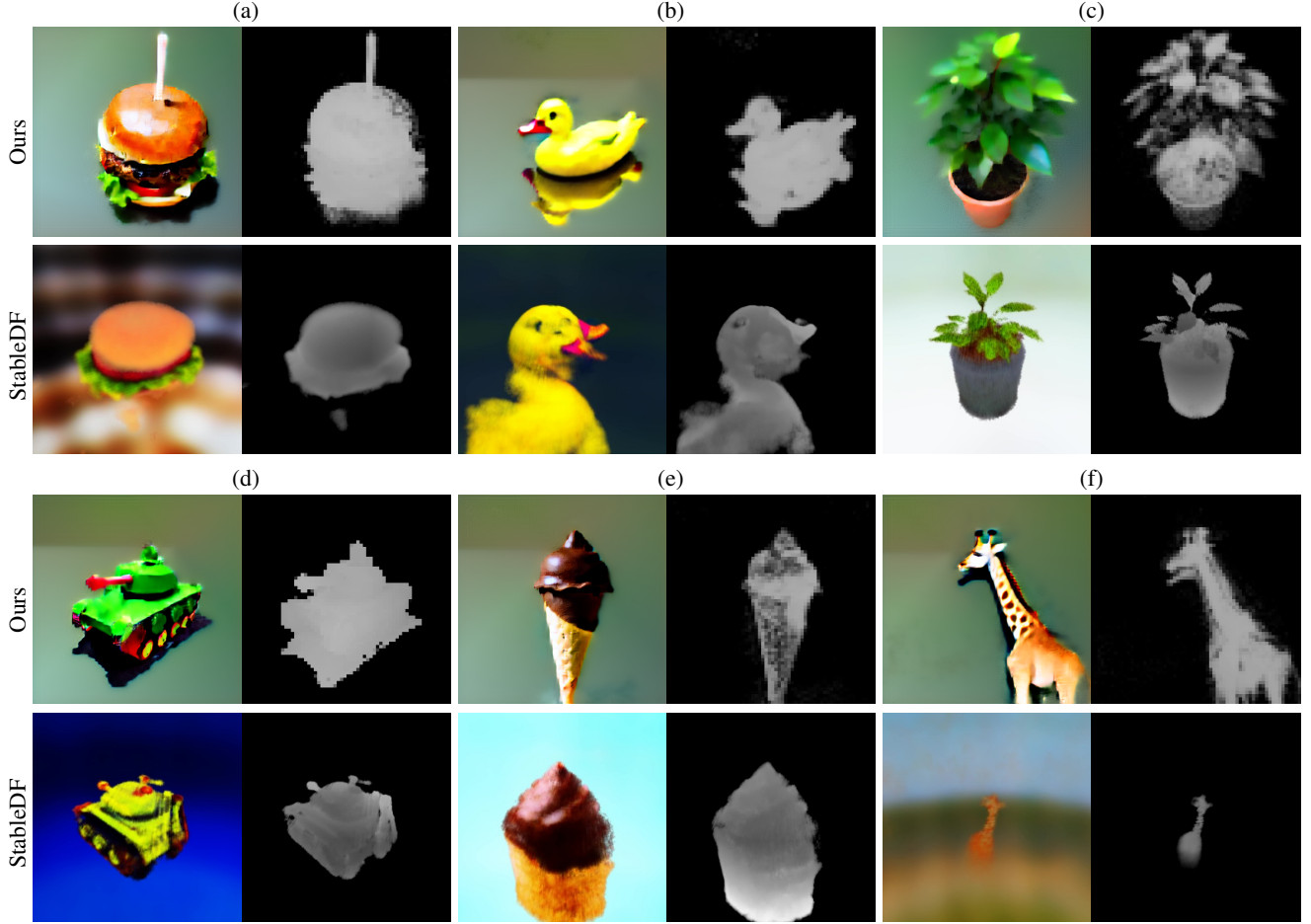


Figure 6. Qualitative comparison between Stable-DreamFusion (StableDF) and Ours. The prompts are: (a) “A high quality photo of a delicious burger”; (b) “a DSLR photo of a yellow duck”; (c) “A ficus planted in a pot”; (d) “A product photo of a toy tank”; (e) “A high quality photo of a chocolate icecream cone”; (f)“A wide angle zoomed out photo of a giraffe”. Both methods are run for 10k iterations without per-prompt finetuning on the hyperparameters. The images on the left are rendered RGB images and the images on the right are depth visualization.

on the vector field produced by PAAS creates high quality images. Here an important decision to make is the schedule of $\{\sigma_i\}$ at which we compute PAAS.

We experimented with an annealed schedule (Annealed σ) vs. a random schedule (Random σ) as proposed in DreamFusion. Under the Annealed σ schedule, we start from a large σ and gradually decrease it as we update the image canvas x . PAAS computed at larger σ level attends to high level image structure while smaller σ provides stronger guidance on detailed features. The Random σ schedule on the contrary uniformly samples a σ at every step. We show qualitative comparisons in Fig. 4.

For unconditioned diffusion models trained on FFHQ, we observe that Annealed σ performs better than Random σ , and the image samples have better pose variation and quality. Particularly, the randomized σ exhibits severe mode-seeking behavior converging to average faces. In the case of LSUN Bedroom, the mode-seeking behavior results in a

blurry image canvas with no content.

On the other hand, natural language prompting plays a critical role when sampling images with Stable Diffusion. When the language guidance is set to a regular level of 3.0, the observations are broadly consistent with sampling on FFHQ and LSUN. Random σ schedule produces blurry outputs. However, when the guidance scale is elevated to 10.0, Random σ schedule begins to generate crisp, clean images and outperforms Annealed σ schedule. Despite various sophisticated strategies on Annealed σ scheduling (see our code for details), at a high language guidance scale Randomized σ remains the better option. We hypothesize that stronger language guidance forces the image distribution to be narrower and more beneficial for a mode-seeking algorithm. We acknowledge none of the images in Fig. 4 can match the sample quality of a standard diffusion inference pipeline, and the right way to apply PAAS as gradient for optimization remains an open problem.

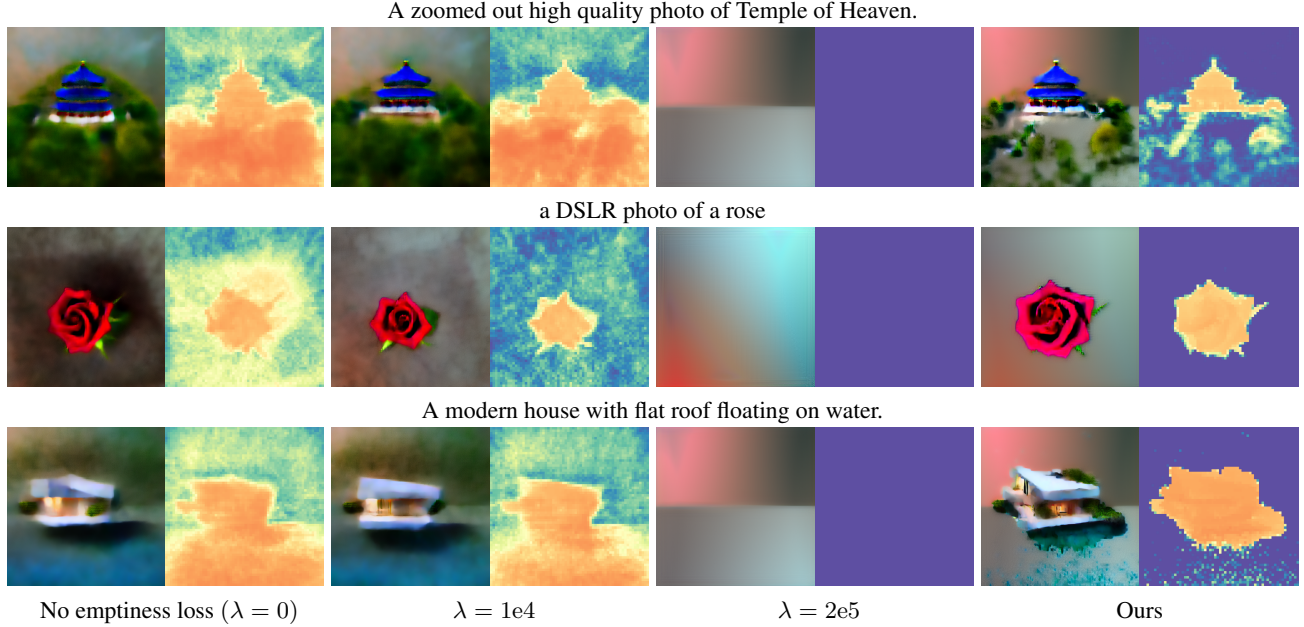


Figure 7. Ablation experiments on the proposed emptiness loss schedule. For each setting of the loss weight λ , we show a rendered image and the associated depth map from a randomly sampled viewpoint. Ours incorporates the loss with weight schedule described in 5.2. It leads to better 3D shape, as evidenced in the cleaner depth maps. Setting the loss weight too low yields "cloudy" depth fields. When setting the weight too high, SJC fails to produce meaningful 3D models.

5.2. 3D Generation

In this paper, we focus on 3D Generation with the language-conditioned Stable Diffusion model. We found that tuning the Annealed σ schedule on FFHQ and LSUN Bedroom in 3D domain is difficult in practice, and leave it as future work. Based on the insights from 2D experiments earlier, we use Random σ schedule coupled with a high language guidance scale.

Rendering with Latent 3D Features. Stable Diffusion economizes compute by performing diffusion modeling on the latent features of a pretrained AutoEncoder. We therefore choose to render a feature image in this latent space from a features field [3, 38] represented by a voxel grid in $\mathbb{R}^{4 \times N_x \times N_y \times N_z}$.

Qualitative Comparison. In Fig. 5, we show text-prompted 3D generation results from SJC. It is capable of generating complex 3D models over a diverse set of prompts ranging from animals to the Sydney Opera House. Next, we compare SJC with Stable-DreamFusion, the third-party implementation based on the same pretrained Stable Diffusion model. In Fig. 6, we show qualitative comparisons of generated 3D assets given the same prompt. We observe that SJC generates 3D models with better image quality and more sensible structure than Stable-DreamFusion in a significant number of cases. We acknowledge that both systems exhibit quality fluctuations over different trials, and the point of this com-

parison is to show that our overall pipeline is competitive.

Ablations. In Fig. 7, we conduct ablations to demonstrate the importance of the proposed emptiness loss and scheduling of its weight λ discussed in Sec. 4.2. We show results without the emptiness loss, with constant weight λ vs our proposed scheduling of λ . We observe that our complete method (Ours) improves the quality of generated 3D models, e.g., fewer floating artifacts and better geometry.

6. Conclusion

We propose an optimization-based approach to generate 3D assets from pretrained image (2D) diffusion models. The key technical contribution is the derivation of Perturb-and-Average Scoring method which bridges the gap between the denoising-trained diffusion models and the non-noisy images encountered in the process of optimizing a 3D model guided by the diffusion. We also propose a new regularization loss for improving the quality of generated 3D scene. Working with the large-scale Stable Diffusion model, we demonstrate that our approach can generate compelling 3D models, comparing favorably to available concurrent work. Finally, we investigate an interesting distinction between the effect of noise scheduling regime in unconditional image diffusion models and a text-conditional model, and identify an avenue for future work.

7. Acknowledgements

The authors would like to thank David McAllester for feedbacks on an early pitch of the work, Shashank Srivastava and Madhur Tulsiani for discussing the $\sqrt{2}$ factor on synthetic experiments. We would like to thank friends at TRI and 3DL lab at UChicago for suggestions on the manuscript. HC would like to thank Kavya Ravichandran for incredible officemate support, and Michael Maire for the discussion and encouragement while riding Metra.

References

- [1] Dmitry Baranchuk, Ivan Rubachev, Andrey Voynov, Valentin Khrulkov, and Artem Babenko. Label-efficient semantic segmentation with diffusion models. *arXiv preprint arXiv:2112.03126*, 2021. 4
- [2] Ruojin Cai, Guandao Yang, Hadar Averbuch-Elor, Zekun Hao, Serge Belongie, Noah Snavely, and Bharath Hariharan. Learning gradient fields for shape generation. In *Eur. Conf. Comput. Vis.*, 2020. 2
- [3] Eric R Chan, Connor Z Lin, Matthew A Chan, Koki Nagano, Boxiao Pan, Shalini De Mello, Orazio Gallo, Leonidas J Guibas, Jonathan Tremblay, Sameh Khamis, et al. Efficient geometry-aware 3D generative adversarial networks. In *IEEE Conf. Comput. Vis. Pattern Recog.*, 2022. 2, 8
- [4] Eric R Chan, Marco Monteiro, Petr Kellnhofer, Jiajun Wu, and Gordon Wetzstein. pi-GAN: Periodic implicit generative adversarial networks for 3d-aware image synthesis. In *IEEE Conf. Comput. Vis. Pattern Recog.*, 2021. 2
- [5] Angel X Chang, Thomas Funkhouser, Leonidas Guibas, Pat Hanrahan, Qixing Huang, Zimo Li, Silvio Savarese, Manolis Savva, Shuran Song, Hao Su, et al. ShapeNet: An information-rich 3D model repository. *arXiv preprint arXiv:1512.03012*, 2015. 2
- [6] Anpei Chen, Zexiang Xu, Andreas Geiger, Jingyi Yu, and Hao Su. Tensorf: Tensorial radiance fields. *arXiv preprint arXiv:2203.09517*, 2022. 2, 5
- [7] Yizong Cheng. Mean shift, mode seeking, and clustering. *IEEE Trans. Pattern Anal. Mach. Intell.*, 1995. 3
- [8] Dorin Comaniciu and Peter Meer. Mean shift analysis and applications. In *Int. Conf. Comput. Vis.*, 1999. 3
- [9] Amélie Deltombe. How much does it cost to create 3D models?, Apr 2022. 2
- [10] Prafulla Dhariwal and Alexander Nichol. Diffusion models beat GANs on image synthesis. In *Adv. Neural Inform. Process. Syst.*, 2021. 2, 6
- [11] Alexandros Graikos, Nikolay Malkin, Nebojsa Jojic, and Dimitris Samaras. Diffusion models as plug-and-play priors. *arXiv preprint arXiv:2206.09012*, 2022. 3
- [12] Jonathan Ho, Ajay Jain, and Pieter Abbeel. Denoising diffusion probabilistic models. In *Adv. Neural Inform. Process. Syst.*, 2020. 1, 2, 3
- [13] Jonathan Ho and Tim Salimans. Classifier-free diffusion guidance. *arXiv preprint arXiv:2207.12598*, 2022. 6
- [14] Fangzhou Hong, Mingyuan Zhang, Liang Pan, Zhongang Cai, Lei Yang, and Ziwei Liu. Avatarclip: Zero-shot text-driven generation and animation of 3D avatars. *arXiv preprint arXiv:2205.08535*, 2022. 2
- [15] Aapo Hyvärinen and Peter Dayan. Estimation of non-normalized statistical models by score matching. *J. Mach. Learn. Res.*, 2005. 1, 3
- [16] Ajay Jain, Ben Mildenhall, Jonathan T Barron, Pieter Abbeel, and Ben Poole. Zero-shot text-guided object generation with dream fields. In *IEEE Conf. Comput. Vis. Pattern Recog.*, 2022. 2
- [17] Nikolay Jetchev. Clipmatrix: Text-controlled creation of 3D textured meshes. *arXiv preprint arXiv:2109.12922*, 2021. 2
- [18] Tero Karras, Miika Aittala, Timo Aila, and Samuli Laine. Elucidating the design space of diffusion-based generative models. *arXiv preprint arXiv:2206.00364*, 2022. 1, 2, 3, 12
- [19] Tero Karras, Samuli Laine, and Timo Aila. A style-based generator architecture for generative adversarial networks. In *IEEE Conf. Comput. Vis. Pattern Recog.*, 2019. 4, 6
- [20] Nasir Khalid, Tianhao Xie, Eugene Belilovsky, and Tiberiu Popa. Clip-mesh: Generating textured meshes from text using pretrained image-text models. *ACM Trans. Graph.*, 2022. 2
- [21] Diederik Kingma, Tim Salimans, Ben Poole, and Jonathan Ho. Variational diffusion models. *Advances in neural information processing systems*, 34:21696–21707, 2021. 1
- [22] Diederik P Kingma and Jimmy Ba. Adam: A method for stochastic optimization. *arXiv preprint arXiv:1412.6980*, 2014. 14
- [23] Sebastian Koch, Albert Matveev, Zhongshi Jiang, Francis Williams, Alexey Artemov, Evgeny Burnaev, Marc Alexa, Denis Zorin, and Daniele Panozzo. ABC: A big cad model dataset for geometric deep learning. In *IEEE Conf. Comput. Vis. Pattern Recog.*, 2019. 2
- [24] Christoph Lassner and Michael Zollhofer. Pulsar: Efficient sphere-based neural rendering. In *IEEE Conf. Comput. Vis. Pattern Recog.*, 2021. 2
- [25] Han-Hung Lee and Angel X Chang. Understanding pure clip guidance for voxel grid nerf models. *arXiv preprint arXiv:2209.15172*, 2022. 2
- [26] Tzu-Mao Li, Miika Aittala, Frédéric Durand, and Jaakko Lehtinen. Differentiable Monte Carlo ray tracing through edge sampling. *ACM Trans. Graph.*, 2018. 2
- [27] Lingjie Liu, Jitao Gu, Kyaw Zaw Lin, Tat-Seng Chua, and Christian Theobalt. Neural sparse voxel fields. In *Adv. Neural Inform. Process. Syst.*, 2020. 2
- [28] Xingchao Liu, Chengyue Gong, Lemeng Wu, Shujian Zhang, Hao Su, and Qiang Liu. Fusedream: Training-free text-to-image generation with improved clip+GAN space optimization. *arXiv preprint arXiv:2112.01573*, 2021. 2
- [29] Matthew M Loper and Michael J Black. OpenDR: An approximate differentiable renderer. In *Eur. Conf. Comput. Vis.*, 2014. 2
- [30] Dimitra Maoutsou, Sebastian Reich, and Manfred Opper. Interacting particle solutions of fokker-planck equations through gradient–log–density estimation. *Entropy*, 2020. 13
- [31] Ricardo Martin-Brualla, Noha Radwan, Mehdi SM Sajjadi, Jonathan T Barron, Alexey Dosovitskiy, and Daniel Duckworth. Nerf in the wild: Neural radiance fields for unconstrained photo collections. In *IEEE Conf. Comput. Vis. Pattern Recog.*, 2021. 2
- [32] Nelson Max. Optical models for direct volume rendering. *IEEE Trans. Vis. Comput. Graph.*, 1995. 2, 5
- [33] Oscar Michel, Roi Bar-On, Richard Liu, Sagie Benaim, and Rana Hanocka. Text2mesh: Text-driven neural stylization for

- meshes. In *IEEE Conf. Comput. Vis. Pattern Recog.*, 2022. 2
- [34] Ben Mildenhall, Pratul P Srinivasan, Matthew Tancik, Jonathan T Barron, Ravi Ramamoorthi, and Ren Ng. Nerf: Representing scenes as neural radiance fields for view synthesis. *Commun. ACM*, 2021. 2, 5
- [35] Thu Nguyen-Phuoc, Chuan Li, Lucas Theis, Christian Richardt, and Yong-Liang Yang. HoloGAN: Unsupervised learning of 3D representations from natural images. In *Int. Conf. Comput. Vis.*, 2019. 2
- [36] Alex Nichol, Prafulla Dhariwal, Aditya Ramesh, Pranav Shyam, Pamela Mishkin, Bob McGrew, Ilya Sutskever, and Mark Chen. Glide: Towards photorealistic image generation and editing with text-guided diffusion models. *arXiv preprint arXiv:2112.10741*, 2021. 2
- [37] Michael Niemeyer and Andreas Geiger. Campari: Camera-aware decomposed generative neural radiance fields. In *Int. Conf. 3DV*, 2021. 2
- [38] Michael Niemeyer and Andreas Geiger. Giraffe: Representing scenes as compositional generative neural feature fields. In *IEEE Conf. Comput. Vis. Pattern Recog.*, 2021. 2, 8
- [39] Merlin Nimier-David, Delio Vicini, Tizian Zeltner, and Wenzel Jakob. Mitsuba 2: A retargetable forward and inverse renderer. *ACM Trans. Graph.*, 2019. 2
- [40] Michael Oechsle, Songyou Peng, and Andreas Geiger. Unisurf: Unifying neural implicit surfaces and radiance fields for multi-view reconstruction. In *Int. Conf. Comput. Vis.*, 2021. 2
- [41] Ben Poole, Ajay Jain, Jonathan T Barron, and Ben Mildenhall. DreamFusion: Text-to-3D using 2D diffusion. *arXiv preprint arXiv:2209.14988*, 2022. 3, 6, 14
- [42] Alec Radford, Jong Wook Kim, Chris Hallacy, Aditya Ramesh, Gabriel Goh, Sandhini Agarwal, Girish Sastry, Amanda Askell, Pamela Mishkin, Jack Clark, et al. Learning transferable visual models from natural language supervision. 2021. 2
- [43] Sai Rajeswar, Fahim Mannan, Florian Golemo, David Vazquez, Derek Nowrouzezahrai, and Aaron Courville. Pix2scene: Learning implicit 3d representations from images. *openreview*, 2018. 2
- [44] Aditya Ramesh, Prafulla Dhariwal, Alex Nichol, Casey Chu, and Mark Chen. Hierarchical text-conditional image generation with clip latents. *arXiv preprint arXiv:2204.06125*, 2022. 2
- [45] Robin Rombach, Andreas Blattmann, Dominik Lorenz, Patrick Esser, and Björn Ommer. High-resolution image synthesis with latent diffusion models. In *IEEE Conf. Comput. Vis. Pattern Recog.*, 2022. 2, 3, 6
- [46] Chitwan Saharia, William Chan, Saurabh Saxena, Lala Li, Jay Whang, Emily Denton, Seyed Kamyar Seyed Ghasemipour, Burcu Karagol Ayan, S Sara Mahdavi, Rapha Gontijo Lopes, et al. Photorealistic text-to-image diffusion models with deep language understanding. *arXiv preprint arXiv:2205.11487*, 2022. 3
- [47] Christoph Schuhmann, Romain Beaumont, Richard Vencu, Cade Gordon, Ross Wightman, Mehdi Cherti, Theo Coombes, Aarush Katta, Clayton Mullis, Mitchell Wortsman, et al. LAION-5B: An open large-scale dataset for training next generation image-text models. *arXiv preprint arXiv:2210.08402*, 2022. 2, 6
- [48] Katja Schwarz, Yiyi Liao, Michael Niemeyer, and Andreas Geiger. GRAF: Generative radiance fields for 3D-aware image synthesis. In *Adv. Neural Inform. Process. Syst.*, 2020. 2
- [49] Jascha Sohl-Dickstein, Eric Weiss, Niru Maheswaranathan, and Surya Ganguli. Deep unsupervised learning using nonequilibrium thermodynamics. In *International Conference on Machine Learning*, pages 2256–2265. PMLR, 2015. 1, 2
- [50] Jiaming Song, Chenlin Meng, and Stefano Ermon. Denoising diffusion implicit models. In *Int. Conf. Learn. Represent.*, 2021. 12
- [51] Yang Song and Stefano Ermon. Generative modeling by estimating gradients of the data distribution. In *Adv. Neural Inform. Process. Syst.*, 2019. 1, 2, 3, 12
- [52] Yang Song and Stefano Ermon. Improved techniques for training score-based generative models. In *Adv. Neural Inform. Process. Syst.*, 2020. 3, 12
- [53] Yang Song, Jascha Sohl-Dickstein, Diederik P Kingma, Abhishek Kumar, Stefano Ermon, and Ben Poole. Score-based generative modeling through stochastic differential equations. In *Int. Conf. Learn. Represent.*, 2021. 1, 2, 3, 13
- [54] Cheng Sun, Min Sun, and Hwann-Tzong Chen. Direct voxel grid optimization: Super-fast convergence for radiance fields reconstruction. In *IEEE Conf. Comput. Vis. Pattern Recog.*, 2022. 2, 5
- [55] Xingyuan Sun, Jiajun Wu, Xiuming Zhang, Zhoutong Zhang, Chengkai Zhang, Tianfan Xue, Joshua B Tenenbaum, and William T Freeman. Pix3D: Dataset and methods for single-image 3D shape modeling. In *IEEE Conf. Comput. Vis. Pattern Recog.*, 2018. 2
- [56] Pascal Vincent. A connection between score matching and denoising autoencoders. *Neural computation*, 2011. 2
- [57] Peng Wang, Lingjie Liu, Yuan Liu, Christian Theobalt, Taku Komura, and Wenping Wang. Neus: Learning neural implicit surfaces by volume rendering for multi-view reconstruction. *arXiv preprint arXiv:2106.10689*, 2021. 2
- [58] Jiajun Wu, Chengkai Zhang, Tianfan Xue, Bill Freeman, and Josh Tenenbaum. Learning a probabilistic latent space of object shapes via 3D generative-adversarial modeling. In *Adv. Neural Inform. Process. Syst.*, 2016. 2
- [59] Zhirong Wu, Shuran Song, Aditya Khosla, Fisher Yu, Liguang Zhang, Xiaoou Tang, and Jianxiong Xiao. 3D ShapeNets: A deep representation for volumetric shapes. In *IEEE Conf. Comput. Vis. Pattern Recog.*, 2015. 2
- [60] Guandao Yang, Xun Huang, Zekun Hao, Ming-Yu Liu, Serge Belongie, and Bharath Hariharan. PointFlow: 3D point cloud generation with continuous normalizing flows. In *Int. Conf. Comput. Vis.*, 2019. 2
- [61] Lior Yariv, Jiatao Gu, Yoni Kasten, and Yaron Lipman. Volume rendering of neural implicit surfaces. In *Adv. Neural Inform. Process. Syst.*, 2021. 2
- [62] Alex Yu, Sara Fridovich-Keil, Matthew Tancik, Qinhong Chen, Benjamin Recht, and Angjoo Kanazawa. Plenoxels: Radiance fields without neural networks. *arXiv preprint arXiv:2112.05131*, 2021. 2, 5
- [63] Fisher Yu, Ari Seff, Yinda Zhang, Shuran Song, Thomas Funkhouser, and Jianxiong Xiao. LSUN: Construction of a large-scale image dataset using deep learning with humans in

- the loop. *arXiv preprint arXiv:1506.03365*, 2015. [6](#)
- [64] Yuxuan Zhang, Wenzheng Chen, Huan Ling, Jun Gao, Yinan Zhang, Antonio Torralba, and Sanja Fidler. Image GANs meet differentiable rendering for inverse graphics and interpretable 3D neural rendering. *arXiv preprint arXiv:2010.09125*, 2020. [2](#)
- [65] Xiaoming Zhao, Fangchang Ma, David Güera, Zhile Ren, Alexander G Schwing, and Alex Colburn. Generative multi-plane images: Making a 2D GAN 3D-Aware. In *Eur. Conf. Comput. Vis.*, 2022. [2](#)

Appendix

- In Sec. A1, we provide diffusion models from a score-based perspective following Karras et al. [18].
- In Sec. A2, we provide additional experiments on our approach, including additional ablation study, qualitative results, and video results.
- In Sec. A3, we document implementation details.

Algorithm 1 Training

```

1: repeat
2:    $\mathbf{x} \sim p_{\text{data}}$ 
3:    $\sigma \sim [\sigma_{\min}, \sigma_{\max}]$ 
4:    $\mathbf{z} \sim \mathcal{N}(0, \mathbf{I})$ 
5:   Take gradient descent step on
       $\nabla_{\phi} \|D_{\phi}(\mathbf{x} + \sigma\mathbf{z}, \sigma) - \mathbf{x}\|^2$ 
6: until converged
7:  $\text{score}(\mathbf{x}, \sigma) = \nabla_{\mathbf{x}} \log p_{\sigma}(\mathbf{x}) = (D_{\phi}(\mathbf{x}, \sigma) - \mathbf{x})/\sigma^2$ 

```

Algorithm 2 Deterministic Sampling

```

1:  $\{\sigma_i\}_{i=1}^T$  descending;  $\sigma_0 = 0$ 
2:  $\mathbf{x}_T = \sigma_T \mathbf{z}$ ,  $\mathbf{z} \sim \mathcal{N}(0, \mathbf{I})$ 
3: for  $t = T, \dots, 1$  do
4:    $\mathbf{x}_{t-1} = \mathbf{x}_t + (\sigma_t - \sigma_{t-1}) \cdot \sigma_t \cdot \text{score}(\mathbf{x}_t, \sigma_t)$ 
5:    $= \underbrace{(1 - w_t) \mathbf{x}_t + w_t D_{\phi}(\mathbf{x}_t, \sigma_t)}_{\text{weighted average}}$   $w_t = \frac{\sigma_t - \sigma_{t-1}}{\sigma_t}$ 
6: return  $\mathbf{x}_0$ 

```

Figure A1. Training and Sampling Algorithm Card for Score-Based Methods with numerical scaling $s(t) = 1$ and $\sigma(t) = t$. Note that the inference step is analogous to DDIM [50], and simplifies to a weighted averaging between the current iterate \mathbf{x}_t and the denoiser output $D(\mathbf{x}_t, \sigma_t)$. This particular scheduling allows for taking large step sizes, and a sample can be generated in as few as 80 network evaluations [18] while maintaining high image quality.

A1. Diffusion Models from Score-Based Perspective

We provide a more detailed recap of diffusion models from the score-based perspective. For a quick overview, we summarize the training and deterministic sampling algorithms in Fig. A1; the deterministic sampling algorithm can be made stochastic by adding noise and adjusting σ level after each update (details see Karras et al. [18]).

In the following analysis we assume that each dimension of the random vector \mathbf{x} is independent, and that the variance in each dimension is 1. The general form of the forward noising step of a diffusion model can be described as scaling and adding noise, *i.e.*

$$\mathbf{x}_t = s(t)\mathbf{x}_0 + s(t)\sigma(t)\mathbf{z}, \quad (28)$$

where $\mathbf{z} \sim \mathcal{N}(0, \mathbf{I})$ and \mathbf{x}_0 is a sample drawn from data distribution. $s(t)$ and $\sigma(t)$ are user-defined coefficients. Here the coefficient on noise \mathbf{z} is parameterized as the product of $s(t)$ and $\sigma(t)$ so that $\sigma(t)$ represents the noise-to-signal ratio in \mathbf{x}_t .

SMLD [51, 52], DDIM [50] and Karras [18] sets scaling, *i.e.* $s(t) = 1$, and therefore adding noise by $\mathbf{x}_0 + \sigma(t)\mathbf{z}$ would cause \mathbf{x}_t to numerically get larger as t increases. DDPM on the other hand introduced rapidly decreasing $s(t)$ to scale down the successive \mathbf{x}_t so that at any time t , $p_t(x)$ has variance fixed at 1. This goal of maintaining a standard deviation 1 requires that

$$\text{Var}[\mathbf{x}_t] = \text{Var}[s(t)\mathbf{x}_0] + \text{Var}[s(t)\sigma(t)\mathbf{z}] \quad (29)$$

$$s(t)^2 \underbrace{\text{Var}[\mathbf{x}_0]}_{=\mathbf{I}} + s(t)^2 \sigma(t)^2 \underbrace{\text{Var}[\mathbf{z}]}_{=\mathbf{I}} = \mathbf{I} \quad (30)$$

$$s(t)^2 + s(t)^2 \sigma(t)^2 = 1 \quad (31)$$

$$\sigma(t) = \sqrt{\frac{1 - s(t)^2}{s(t)^2}} \quad (32)$$

DDPM specifies the $s(t)$ by a set of β_t , *i.e.*, $s(t) = \sqrt{\bar{\alpha}_t} = \sqrt{\prod_{i \leq t} \alpha_i} = \sqrt{\prod_{i \leq t} (1 - \beta_i)}$, and therefore $\sigma(t) = \sqrt{\frac{1 - \bar{\alpha}_t}{\bar{\alpha}_t}}$.

The noising step (28) describes the marginal distribution at $p_t(\mathbf{x})$. The infinitesimal time evolution of this process can be written as the following stochastic differential equation [53]:

$$d\mathbf{x} = f(t)\mathbf{x} dt + g(t) d\omega_t \quad \text{where} \quad f(t) = \frac{\dot{s}(t)}{s(t)} \quad g(t) = s(t)\sqrt{2\dot{\sigma}(t)\sigma(t)}. \quad (33)$$

Fokker-Planck equation [30] states that a stochastic differential equation of the form (33) is identified with a partial differential equation describing the marginal probability density distribution $p_t(\mathbf{x})$

$$d\mathbf{x} = f(x, t) dt + g(t) d\omega_t \longleftrightarrow \frac{\partial p_t(\mathbf{x})}{\partial t} = -\nabla \cdot \left[f(x, t) p_t(\mathbf{x}) - \frac{g(t)^2}{2} \nabla_x p_t(\mathbf{x}) \right]. \quad (34)$$

Applying this identity tells us that a stochastic differential equation like (33) implies a deterministic, ordinary differential equation. Here we illustrate the proof schematically:

$$\begin{aligned} d\mathbf{x} &= \underbrace{f(t)\mathbf{x} dt + g(t) d\omega_t}_{\text{stochastic}} \xrightarrow{\text{FP}} \frac{\partial p_t(\mathbf{x})}{\partial t} = -\nabla \cdot \left[f(t)\mathbf{x} p_t(\mathbf{x}) - \frac{g(t)^2}{2} \nabla_x p_t(\mathbf{x}) \right] \\ &\quad \downarrow \text{implies} \\ d\mathbf{x} &= \underbrace{\left(f(t)\mathbf{x} - \frac{g(t)^2}{2} \nabla_x \log p_t(\mathbf{x}) \right) dt + 0 d\omega_t}_{\text{deterministic}} \xleftarrow{\text{FP}} \frac{\partial p_t(\mathbf{x})}{\partial t} = -\nabla \cdot \left[\left(f(t)\mathbf{x} - \frac{g(t)^2}{2} \nabla_x \log p_t(\mathbf{x}) \right) p_t(\mathbf{x}) - 0 \right] \end{aligned} \quad (35)$$

The application of the log derivative trick is expanded below:

$$\frac{\partial p_t(\mathbf{x})}{\partial t} = -\nabla \cdot \left[f(t)\mathbf{x} p_t(\mathbf{x}) - \frac{g(t)^2}{2} \nabla_x p_t(\mathbf{x}) \right] \quad (36)$$

$$= -\nabla \cdot \left[\frac{f(t)\mathbf{x} p_t(\mathbf{x}) - \frac{g(t)^2}{2} \nabla_x p_t(\mathbf{x})}{p_t(\mathbf{x})} p_t(\mathbf{x}) \right] \quad (37)$$

$$= -\nabla \cdot \left[\left(f(t)\mathbf{x} - \frac{g(t)^2}{2} \underbrace{\frac{\nabla_x p_t(\mathbf{x})}{p_t(\mathbf{x})}}_{\text{log derivative}} \right) p_t(\mathbf{x}) \right] \quad (38)$$

$$= -\nabla \cdot \left[\left(f(t)\mathbf{x} - \frac{g(t)^2}{2} \nabla_x \log p_t(\mathbf{x}) \right) p_t(\mathbf{x}) \right]. \quad (39)$$

Substituting the expression for $f(t)$ and $g(t)$ from (33), we obtain an ODE from which we can sample the data by applying the score function with a step schedule that theoretically guarantees to take us back to initial, clean data distribution

$$d\mathbf{x} = \frac{\dot{s}(t)}{s(t)} \mathbf{x} - \frac{1}{2} \left(s(t) \sqrt{2\dot{\sigma}(t)\sigma(t)} \right)^2 \nabla_x \log p_t(\mathbf{x}) dt \quad (40)$$

$$d\mathbf{x} = \frac{\dot{s}(t)}{s(t)} \mathbf{x} - s(t) \frac{\dot{\sigma}(t)}{\sigma(t)} \left(D(\mathbf{x}/s(t); \sigma(t)) - \mathbf{x}/s(t) \right) dt. \quad (41)$$

When $s(t) = 1, \sigma(t) = t$, the above simplifies to

$$d\mathbf{x} = -\sigma_t \cdot \frac{D(\mathbf{x}; \sigma_t) - \mathbf{x}}{\sigma_t^2} dt \quad (42)$$

$$d\mathbf{x} = -\sigma_t \cdot \text{score}(\mathbf{x}, \sigma_t) dt \quad (43)$$

Note that this schedule with $s(t) = 1, \sigma(t) = t$ allows for taking large step sizes during inference since it introduces no extra curvature in the trajectory beyond what's induced by the score function itself. The discretized sampling algorithm of equation (43) is described in Fig. A1.

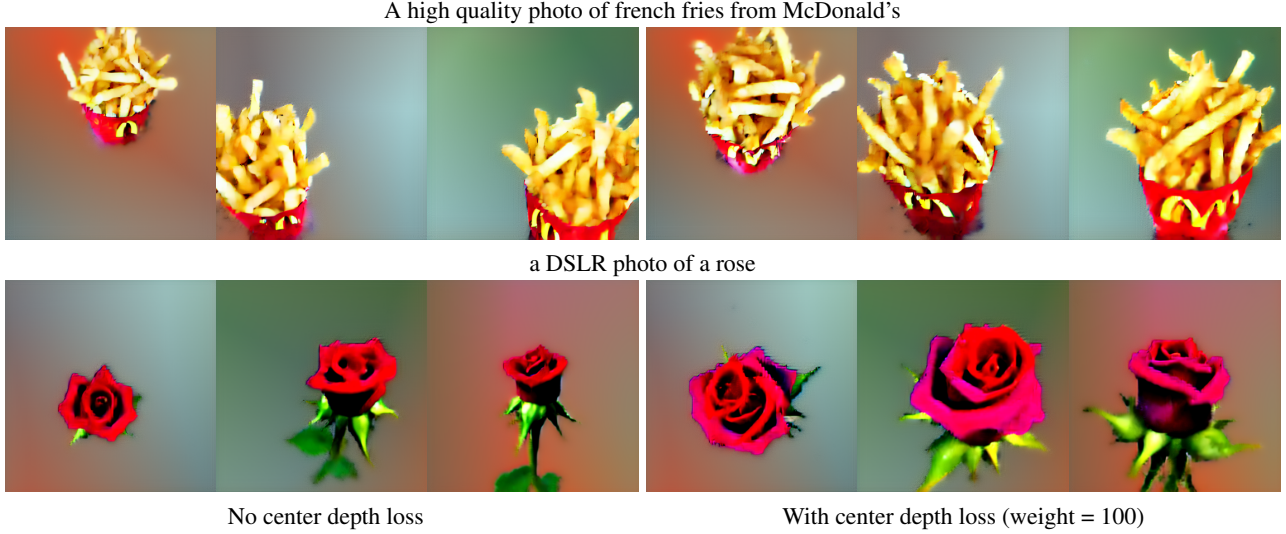


Figure A2. Ablation experiments on the proposed center depth loss. Each pair of corresponding columns of the same prompt are visualized from the same camera angle.

A2. Additional Experiments

Ablation on center depth loss. In Fig. A2, we illustrate the effect of the center depth loss proposed in Eq. (27). Without the center depth loss, we observe that some objects, *e.g.*, French Fries, are placed far from the center of the scene box and tend to drift around when the camera viewpoints are changed. This effect is more pronounced in the provided video result. In contrast, a moderate center depth loss forces the object to be placed at the scene box center. Additionally, we observe that the objects tend to be enlarged to occupy more of the visible screen space without wasting model capacity.

Additional qualitative results. We provide additional qualitative results from SJC in Fig. A3. Note that we increase the resolution of the depth maps beyond the 64×64 resolution of the image latents by rendering subpixel rays. In general, we observe that the volumetric renderer is powerful enough to hallucinate shadows (horse), water surfaces (Sydney opera house, duck), grasslands (zebra) and even a traffic lane (school bus), using the volume densities.

Video results. We have attached numerous video results in the supplemental materials. Please see the attached HTML and videos. We have named each file after the text prompt used to generate the 3D asset. In addition, we included the videos for the ablation experiments in Fig. 7 and Fig. A2.

A3. Implementation Details

3D scene setup. Our voxel grids are of size 100^3 , and placed at world origin with a normalized side length $[-1, 1]^3$. We sample cameras uniformly on a hemisphere that covers the voxel cube with a radius of 1.5, with look-at directions pointing at the origin. The camera field of view is randomly sampled from 40 degrees to 70 degrees during optimization, and fixed to 60 degrees at test time. We found the jittering on FoV to help with 3D optimization in some cases, and this data augmentation technique is reported in DreamFusion [41]. Our scene background consists of an optimizable image of size 4×4 environment-mapped to the spherical surface by azimuth and elevation angles of the incoming ray. The small image size with constrained capacity helps to avoid confounding visual artifacts accumulating in the background during optimization.

Optimization. We use Adamax [22] optimizer and perform gradient descent at a learning rate of 0.05 for 10,000 steps, with some prompts running at a longer schedule for better quality. Note that when performing gradient descent with NEScore, we implicitly rely on the optimizer’s momentum state to perform the averaging. We have tried explicitly averaging the scores at multiple noise perturbations, but observed no benefits or degradation. The language-guidance scale is set to 100. Our system consumes 9GB of GPU memory during optimization, and takes approximately 25 minutes on an A6000 GPU including the time spent on miscellaneous tasks like visualization.

View-dependent prompting. An influence of DreamFusion [41] on our work is the use of view-dependent prompting. Language prompts are prepended with one of the following: “overhead view of”, “front view of”, “backside view of”, “side

view of” depending on the camera location. More specifically, when camera elevation is above 30 degrees we use the “overhead view” prompt. Otherwise, the prompts are assigned based on the azimuth quadrant the camera falls into. This technique helps to alleviate the degeneracy of multiple frontal faces being painted around an object during optimization. We hope as part of our future work to develop a more general solution to induce the optimization towards more plausible geometry without using language as guidance.



Figure A3. Additional results of text-prompted generation of 3D models with SJC.